The Astrophysical Journal, 755:171 (13pp), 2012 August 20 doi:10.1088/0004-637X/755/2/171

[C II] 158 μm LUMINOSITIES AND STAR FORMATION RATE IN DUSTY STARBURSTS AND ACTIVE GALACTIC NUCLEI*

L. Sargsyan[1], V. Lebouteiller[2], D. Weedman[1], H. Spoon[1], J. Bernard-Salas[3], D. Engels[4], G. Stacey[1], J. Houck[1], D. Barry[1], J. Miles[5], and A. Samsonyan[6]
[1] Astronomy Department, Cornell University, Ithaca, NY 14853, USA; sargsyan@isc.astro.cornell.edu, dweedman@isc.astro.cornell.edu
[2] Laboratoire AIM, CEA/DSM-CNRS-Universite Paris Diderot, DAPNIA/Service d'Astrophysique, Saclay, France; vianney.lebouteiller@cea.fr
[3] Institut d'Astrophysique Spatiale, Universite Paris Sud 11, 91405 Orsay, France
[4] Hamburger Sternwarte, Hamburg, Germany
[5] USRA/SOFIA, NASA Ames Research Center, Moffett Field, CA, USA
[6] Byurakan Astrophysical Observatory, Byurakan, Armenia
Received 2012 May 2; accepted 2012 June 21; published 2012 August 7

ABSTRACT

Results are presented for [C II] 158 μm line fluxes observed with the *Herschel* PACS instrument in 112 sources with both starburst and active galactic nucleus (AGN) classifications, of which 102 sources have confident detections. Results are compared with mid-infrared spectra from the *Spitzer* Infrared Spectrometer and with $L_{\rm ir}$ from *IRAS* fluxes; AGN/starburst classifications are determined from equivalent width of the 6.2 μm polycyclic aromatic hydrocarbon (PAH) feature. It is found that the [C II] line flux correlates closely with the flux of the 11.3 μm PAH feature independent of AGN/starburst classification, $\log [f([\mathrm{C\,II}]\ 158\ \mu\mathrm{m})/f(11.3\ \mu\mathrm{m\ PAH})] = -0.22 \pm 0.25$. It is concluded that the [C II] line flux measures the photodissociation region associated with starbursts in the same fashion as the PAH feature. A calibration of star formation rate (SFR) for the starburst component in any source having [C II] is derived comparing [C II] luminosity $L([\mathrm{C\,II}])$ to $L_{\rm ir}$ with the result that $\log \mathrm{SFR} = \log L([\mathrm{C\,II}]) - 7.08 \pm 0.3$, for SFR in $M_\odot\ \mathrm{yr}^{-1}$ and $L([\mathrm{C\,II}])$ in $L_\odot$. The decreasing ratio of $L([\mathrm{C\,II}])$ to $L_{\rm ir}$ in more luminous sources (the "[C II] deficit") is shown to be a consequence of the dominant contribution to $L_{\rm ir}$ arising from a luminous AGN component because the sources with the largest $L_{\rm ir}$ and smallest $L([\mathrm{C\,II}])/L_{\rm ir}$ are AGNs.

Key words: galaxies: active – galaxies: distances and redshifts – galaxies: starburst – infrared: galaxies

1. INTRODUCTION

Understanding the initial formation of galaxies depends on discovering sources obscured by dust and tracing these sources to their earliest epoch in the universe. The extreme luminosity of dusty, local sources was originally revealed by the ultraluminous infrared galaxies (ULIRGs; e.g., Soifer et al. 1987; Sanders & Mirabel 1996), whose luminosity arises from infrared emission by dust, and this dust often obscures the primary optical sources of luminosity. That such galaxies are important in the early universe was demonstrated by source modeling which indicated that the infrared dust emission from galaxies dominates the cosmic background luminosity (Chary & Elbaz 2001; Lagache et al. 2004; Le Floc'h et al. 2005).

Surveys in the submillimeter were the first to discover individual, optically obscured, dusty sources at redshifts $z \gtrsim 2$ (Chapman et al. 2005). A variety of observing programs using spectra from the *Spitzer* Infrared Spectrometer (IRS; Houck et al. 2004) subsequently found luminous ULIRGs to redshifts $z \sim 3$ (e.g., Houck et al. 2005; Yan et al. 2007; Sajina et al. 2007; Weedman & Houck 2009b). This *Spitzer*-discovered population of high-redshift ULIRGs has large infrared-to-optical flux ratios [$f_\nu(24\ \mu\mathrm{m}) > 1$ mJy and $R > 24$] attributed to heavy extinction by dust and has been labeled "dust obscured galaxies" (DOGs; Dey et al. 2008). Some DOGs are powered primarily by starbursts and some by active galactic nuclei (AGNs), and the DOGs are similar to the population of submillimeter galaxies in overall spectral energy distributions (SEDs), redshifts, and luminosities (Alexander et al. 2005; Pope et al. 2008; Menendez-Delmestre et al. 2009; Coppin et al. 2010; Kovacs et al. 2010).

To discover and understand dusty galaxies at even higher redshifts than the DOGs known so far, the atomic line emission of [C II] 158 μm is the single most important spectroscopic feature because it is the strongest far-infrared line (Stacey et al. 1991; Luhman et al. 2003; Brauher et al. 2008). As a consequence, this line will provide the best opportunity for redshift determinations and source diagnostics using submillimeter and millimeter spectroscopic observations. Already, [C II] has been detected at redshift exceeding 7 (Maiolino et al. 2005; Venemans et al. 2011) and shown to be strong in starbursts with $1 < z < 2.5$ (Hailey-Dunsheath et al. 2010; Stacey et al. 2010; Ivison et al. 2010).

Our primary motives for the present paper are to present [C II] results for a large sample of dusty sources and to compare with mid-infrared classification indicators for starbursts and AGNs. This comparison leads to a calibration between star formation rate (SFR) and [C II] luminosity. We emphasize the diagnostics used for DOGs at $z \sim 2$, because the large populations of submillimeter and mid-infrared DOGs now known at this epoch provide a crucial reference for scaling to higher redshifts. The epoch $2 \lesssim z \lesssim 3$ is also important because this is the observed epoch at which starburst and AGN activity seems to peak (e.g., Madau et al. 1998; Reddy & Steidel 2009; Fan et al. 2004; Croom et al. 2004; Brown et al. 2006).

The [C II] line should be primarily a diagnostic of star formation, being associated with the photodissociation region (PDR) surrounding starbursts (Tielens & Hollenbach 1985; Helou et al. 2001; Malhotra et al. 2001; Meijerink et al. 2007), and the line appears to be weaker in the most luminous sources ("the [C II] deficit"; Luhman et al. 2003). It is crucial

* Based on observations with the *Herschel Space Observatory*, which is an ESA space observatory with science instruments provided by European-led Principal Investigator consortia and with important participation from NASA.

to understand the origin of this line and the extent to which its luminosity is a measure of SFR. Does [C II] scale with other star formation indicators? Is the [C II] deficit a consequence of AGN dominance rather than star formation in luminous sources? Determining such answers is the objective of new observations we have undertaken with the *Herschel Space Observatory* (Pilbratt et al. 2010).

2. OBSERVATIONS

2.1. Selection of Sources

Using the *Herschel* PACS instrument (Poglitsch et al. 2010), it is now possible to measure efficiently the [C II] luminosity in luminous, dusty galaxies within the local universe. Many observations are underway (e.g., the SHINING key program, PI: E. Sturm). Our *Herschel* PACS observing program (OT1dweedman1) includes 112 sources chosen to connect the [C II] results to various mid-infrared diagnostics of starburst and AGN activity that can be derived from spectroscopic observations with the *Spitzer* IRS.

Our source list was assembled using these criteria. (1) All targets have complete low-resolution and high-resolution mid-infrared spectra from 5 μm to 35 μm with the *Spitzer* IRS; low-resolution spectra are available in the Cornell Atlas of *Spitzer* IRS Spectra (CASSIS; Lebouteiller et al. 2011[7]). (2) All targets have complete fluxes from the *Infrared Astronomical Satellite* (*IRAS*) so the total infrared luminosities $L_{\rm ir}$ can be determined with the relation of Sanders & Mirabel (1996). (3) Finally, all targets are spatially unresolved (according to estimates described below) to give confidence that IRS and *Herschel* spectroscopy measure the same source. These selection criteria do not include any source classification criteria; the criteria derive only from selection based on available archival observations.

The 112 sources in our observing program are taken from the 301 sources in Sargsyan et al. (2011) by proceeding as follows. That list was produced starting with all IRS archival observations then available having both IRS low-resolution spectra and complete flux measures with *IRAS*, giving a sample of 501 sources. To exclude extended sources for which IRS and *IRAS* flux comparisons would not be the same, the total f_ν(*IRAS* 25 μm) was compared to the f_ν(IRS 25 μm) measured with the 10″ slit of the IRS to define a list of 301 sources estimated to be unresolved (see Figure 2 in Sargsyan et al. 2011 and the accompanying discussion). The resulting sample has $0.004 < z < 0.34$ and $42.5 < \log L_{\rm IR} < 46.8$ (erg s^{-1}) and covers the full range of starburst galaxy and AGN classifications.

Of these 301 sources, 182 also have IRS high-resolution spectra in addition to the low-resolution spectra. At the time of our PACS proposal, 41 of these 182 had PACS observations listed either in the *Herschel* Reserved Observations Search Tool (30 sources) or archival [C II] data from *Infrared Space Observatory* (*ISO*; 11 sources; Brauher et al. 2008). Of the 141 remaining sources, we selected for new PACS [C II] observations the 123 brightest as measured by IRS flux of the 11.3 μm polycyclic aromatic hydrocarbon (PAH) feature. Subsequently, 11 of these 123 were yielded to program OT1dfarrah1, giving our final sample of 112 sources. These are the results we report in the present paper. We also include for comparison the prototype ULIRG Markarian 231 using the PACS [C II] flux from Fischer et al. (2010) and IRS data from Sargsyan et al. (2011) because this important source satisfies all of our sample selection criteria.

[7] http://cassis.astro.cornell.edu/atlas; CASSIS is a product of the Infrared Science Center at Cornell University.

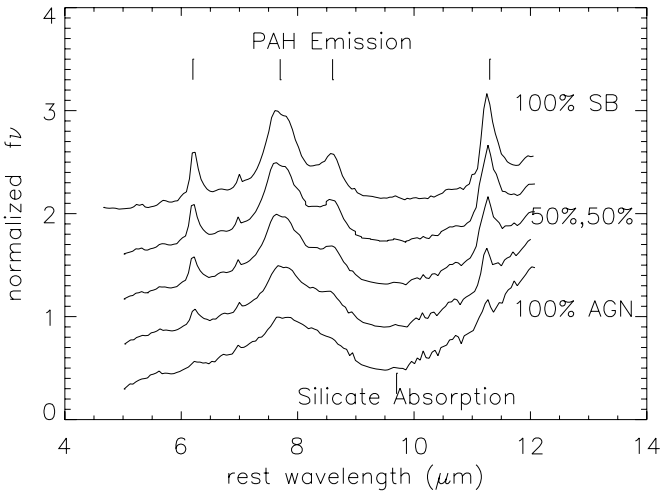

Figure 1. Transition in mid-infrared spectra from pure starburst to pure absorbed AGN. Top spectrum is median observed rest-frame IRS spectrum of 51 starburst PAH emission sources (100% starburst) from samples in Sargsyan et al. (2011); bottom spectrum is median observed rest-frame IRS spectrum of 65 AGNs with silicate absorption (100% AGN; from the same reference); intermediate spectra show mixes of top and bottom spectra, changing mix by 25% in each spectrum. Spectra are normalized to peak f_ν(7.8 μm) and displaced by 0.5 units of f_ν.

Having IRS low-resolution and high-resolution spectra for all sources means that many comparisons can be made with various mid-infrared diagnostic features, including several atomic and molecular emission lines, silicate absorption and emission, and the dust continuum. In future papers, we will present comparisons with emission line fluxes, velocities, and profiles. For the present analysis, our goal is only to compare the [C II] results to PAH molecular emission features. The PAH features are the most important diagnostics for classifying dusty, luminous starbursts, and AGNs at $z \gtrsim 2$, as described below in Section 2.2 and illustrated in Figure 1. They are also the most important mid-infrared measure of SFR. By relating [C II] to PAH, the populations of DOGs already known at $z \sim 2$ can be compared with sources at even higher redshifts when such sources are observed using [C II].

2.2. Classification of Sources

To understand the ultimate luminosity source, it is necessary to distinguish starbursts and AGNs. The most important mid-infrared spectroscopic criterion for classification is the broad complex of PAH emission (Figure 1) which arises within the PDR surrounding starbursts (Peeters et al. 2004). That PAH emission is weak in AGNs compared to starbursts was initially demonstrated observationally by Genzel et al. (1998) using spectroscopy with the *ISO*. The strength of a PAH feature compared to the underlying continuum (the equivalent width, EW) decreases as the AGN component increases because the continuum beneath the PAH feature increases in proportion to the hot dust heated by the AGN.

Spectra for hundreds of sources with the IRS quantified the dependence of PAH strength on starburst/AGN classification determined from optical spectra (e.g., Brandl et al. 2006; Weedman & Houck 2009a; Sargsyan et al. 2011). These comparisons with optical classifications led to an infrared classification derived from EW (6.2 μm), measured as described below. The continuous gradation of EW (6.2 μm) provides a single

parameter, the quantitative measure of the starburst/AGN mix. We use the EW (6.2 μm) for classification rather than the stronger 11.3 μm PAH feature because the 11.3 μm feature is near the long wavelength limit of the IRS for $z \gtrsim 2$, and we also want to apply the classification at high redshifts.

The PAH spectroscopic emission features are complex (Figure 1), including an underlying plateau between 5 μm and 10 μm, a maximum at rest-frame ~7.7 μm, and specific features at 6.2 μm and 11.3 μm. Features are broad and blended, and the "continuum" beneath the features includes wings of other PAH emission features. Sophisticated measures of PAH strengths require various assumptions about the underlying dust continuum and relative feature strengths to deconvolve the full, broad PAH features into different components (Smith et al. 2007). This deconvolution is uncertain when using observations of faint sources with poor signal-to-noise ratios (S/Ns) and limited coverage of rest-frame wavelengths, as arises for the highest redshift sources with IRS spectra.

To avoid such uncertainties, we use simple parameters for PAH strength that allow consistent, model-independent observational measures that are possible even with weak features or poor S/Ns. These measures are made with the SMART software for IRS spectra (Higdon et al. 2004) and are (1) the EW (6.2 μm) determined using a Gaussian fit to the PAH feature and a linear fit to the continuum beneath the feature within the range 5.5 μm to 6.9 μm; (2) the total flux of the 11.3 μm feature, f(11.3 μm), determined with a Gaussian fit to the PAH feature and a linear fit to the continuum beneath the feature from 10.5 μm to 12 μm. Measurements are given in Sargsyan et al. (2011).

Although the range of EW (6.2 μm) is continuous among spectra, comparisons with optical classes show consistent divisions. The initial study of IRS spectra for 22 optically classified starbursts showed that 21 of 22 sources have rest-frame EW (6.2 μm) > 0.4 μm (Brandl et al. 2006). Subsequent studies confirmed this result and also determined an EW limit for optically classified AGNs. Of the 19 sources with EW (6.2 μm) > 0.4 μm having optical classifications in the f_ν(24 μm) > 10 mJy sample of Weedman & Houck (2009a), 18 are classified as starbursts; of the 17 sources with EW (6.2 μm) < 0.1 μm, 16 are classified as AGNs. The distribution in Sargsyan et al. (2011) is illustrated in their Figure 4, where 14 of 17 sources having both EW (6.2 μm) > 0.4 μm and optical classifications are starbursts, and 42 of 57 having EW (6.2 μm) < 0.1 μm are AGNs. Using these results, we have adopted the criteria that AGNs have EW (6.2 μm) < 0.1 μm, composite sources have intermediate 0.1 μm < EW (6.2 μm) < 0.4 μm, and starbursts have EW (6.2 μm) > 0.4 μm. (Observed frame EWs are greater by a factor of (1 + z) compared to rest-frame EWs.)

This empirical observational classification is quantitatively consistent with starburst/AGN luminosity fractions when synthetic spectral combinations of mid-infrared spectral templates are assumed. Using the mixes of observed starburst and AGN spectra shown in Figure 1, for example, the dependence of EW (6.2 μm) on the fractional AGN contribution to the mid-infrared luminosity is shown in Figure 2. With this mix of spectra, >90% of the mid-infrared luminosity arises from a starburst if EW (6.2 μm) > 0.4 μm, confirming that this value of EW (6.2 μm) defines a starburst. The majority of the mid-infrared luminosity, >55%, arises from an AGN if EW (6.2 μm) < 0.1 μm. In fact, most AGNs in the present paper actually have EW (6.2 μm) < 0.01 μm for which >90% of the luminosity arises from an AGN in Figure 2. Composite sources have contributions from both starburst and AGN. The

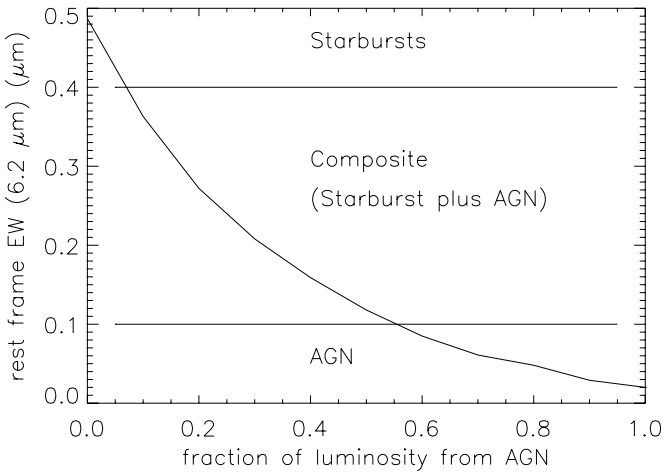

Figure 2. Equivalent width in μm of 6.2 μm PAH emission feature shown in Figure 1 compared to a fraction of total luminosity at 7.8 μm which arises from AGN component. Curve derives from various mixtures of the "100% starburst" and "100% AGN" spectra shown in Figure 1. Criteria for EW (6.2 μm) used to classify *Herschel* sources in the remaining figures are illustrated.

boundaries illustrated in Figure 2, therefore, are those used to define classification symbols in those figures below which do not display a quantitative EW (6.2 μm).

2.3. Observations and [C II] Measurements

All [C II] observations were made using PACS line spectroscopy in point-source chop nod mode with medium throw. A single repetition cycle was used for all but 20 sources, giving total observing time for the program of 20.2 hr for 112 sources. Table 1 includes results for the 112 sources. Data reduction was done with version 8 of the *Herschel* Interactive Processing Environment, together with the "PACSman" software (Lebouteiller et al. 2012) used for fitting line profiles and continuum within each of the 25 equivalent spatial pixels, or "spaxels," produced by the PACS image slicer.[8] Illustrations of these fits are in Figure 3, with examples of both high and low S/N sources, together with an example of a source with an unusually broad line profile.

We include a line detection as real if the S/N for the line profile fit in the brightest spaxel exceeds 3. If S/N < 3 for the line flux in the brightest spaxel, we adopt an upper limit for the total line flux. Of our 112 sources, 102 are detected according to this criterion. All results are in Table 1.

One method for measuring total source fluxes with PACS is to take only fluxes in the brightest, central spaxel and correct to total flux assuming an unresolved source that is perfectly centered in the central spaxel. In this case, the flux from the central spaxel is corrected by a factor of 1.95 at wavelength 160 μm to determine the total flux.[9] The greatest uncertainties in this technique are the requirement of perfect centering and the possibility that sources are extended.

To minimize centering uncertainties and to maximize the inclusion of total flux, the procedure we adopt instead for measuring detections is to measure the total line flux in the brightest spaxel plus the 8 surrounding spaxels, $f(3 \times 3)$. (For detected sources, we find that the brightest spaxel is always the central spaxel, except for four cases where it is displaced by one spaxel, noted in Table 1.) The $f(3 \times 3)$ covers a spatial area

[8] http://herschel.esac.esa.int/Docs/PACS/pdf/pacs_om.pdf
[9] http://herschel.esac.esa.int/twiki/pub/Public/PacsCalibrationWeb/PacsSpectroscopyPerformanceAndCalibration_31May2011.pdf

Table 1
[C II] Line Fluxes and Luminosities

No.	Name	Coordinates	z	EW[a]	f[C II][b]	S/N[c]	[C II]/11.3[d]	[C II]/7.8[e]	$L_{\rm C\,II}$[f]	$L_{\rm C\,II}/L_{\rm ir}$[g]	*Herschel* ID
				6.2 μm					Solar		
		J2000		(μm)	(W m^{-2})		log	log	log	log	
1	Mrk0334	000309.62+215736.6	0.0219	0.248	6.70e-16	169	−0.26	−2.27	8.27	−2.81	1342235847
2	MCG-02-01-051/2	001850.90−102236.7	0.0271	0.558	1.18e-15	4.9	−0.17	−2.09	8.70	−2.75	1342235846
3	IRAS00199−7426	002207.01−740941.7	0.0964	0.351	1.98e-16	51	−0.29	−2.30	9.05	−3.27	1342237574
4	E12-G21	004046.10−791424.0	0.0330	0.278	5.76e-16	5.7	−0.12[l]	−2.04	8.48	−2.54	1342232583
5	IRASF00456−2904SW	004806.75−284818.6	0.1103	0.428	1.26e-16	44	−0.25	−2.19	8.98	−3.23	1342238141
6	MCG-03-04-014	011008.93−165109.9	0.0350	0.455	1.38e-15	5.2	−0.25	−2.14	8.95	−2.67	1342238385
7	NGC 0454	011424.90−552352.0	0.0122	0.008[k]	1.55e-16	5.2	−0.31	−2.51	7.11	−3.14	1342232616
8	ESO244-G012	011808.31−442743.4	0.0229	0.536	1.14e-15	188	−0.32	−2.26	8.53	−2.86	1342234998
9	ESO353-G020	013451.26−360814.4	0.0159	0.404	1.56e-15	249	−0.18	−2.19	8.35	−2.68	1342238600
10	IRASF01364−1042	013852.91−102711.0	0.0482	0.306	1.32e-16	6.0	−0.05	−2.27	8.26	−3.54	1342238601
11	UGC01385	015453.82+365504.3	0.0188	0.538	5.70e-16	146	−0.44	−2.29	8.06	−2.97	1342237475
12	NGC 0788	020106.45−064855.9	0.0136	<0.003[k]	8.43e-17	4.8	0.12	−2.56	6.95	−3.18	1342238364
13	IRAS02054+0835[j]	020806.90+085004.3	0.3450	0.024[k]	<2.00e-17	0.1	<−0.30	<−2.88	<9.26	<−3.80	1342239376
14	Mrk0590[j]	021433.56−004600.1	0.0264	<0.007	2.06e-16	3.5	0.84	−1.86	7.92	−2.75	1342238636
15	UGC01845	022407.97+475811.9	0.0156	0.443	1.42e-15[i]	3.4	−0.37	−2.32	8.29	−2.80	1342239504
16	IC1816	023151.00−364019.4	0.0169	0.031[k]	3.42e-16	52	0.12	−1.89	7.75	−2.72	1342239370
17	NGC 0973	023420.11+323020.2	0.0162	<0.002[k]	2.46e-16[i]	3.9	0.47	−2.05	7.56	−2.89	1342239500
18	IRASF02437+2122	024639.13+213510.4	0.0233	0.155	1.50e-16	44	−0.42	−2.50	7.67	−3.49	1342239499
19	UGC02369	025401.84+145815.7	0.0312	0.434	8.21e-16[i]	174[h]	−0.10	−2.08	8.66	−2.96	1342239497
20	Mrk1066	025958.59+364914.3	0.0120	0.249	9.39e-16	4.9	−0.46	−2.30	7.89	−3.04	1342238915
21	IRASF03217+4022	032505.37+403332.2	0.0234	0.406	5.96e-16[i]	3.7	−0.29	−2.21	8.27	−3.04	1342238940
22	Mrk0609	032525.34−060838.7	0.0345	0.318	5.44e-16	4.0	−0.31	−2.12	8.57	−2.81	1342239752
23	IRASF03359+1523	033847.07+153254.1	0.0354	0.358	4.60e-16	5.0	−0.04	−1.93	8.52	−3.04	1342238916
24	IRASF03450+0055	034740.18+010514.0	0.0310	<0.001	2.69e-17	6.8	> −0.42	−3.33	7.17	−3.87	1342238943
25	IRAS03538−6432	035425.23−642344.5	0.3007	0.079[k]	<2.00e-17	2.4	<−0.55	<−2.73	<9.13	<−3.64	1342223119
26	IRAS04103−2838	041219.53−283024.4	0.1175	0.182	8.53e-17	23.5	−0.41	−2.46	8.87	−3.33	1342239509
27	IRAS04114−5117	041244.92−510934.2	0.1250	0.338	6.32e-17	4.4[h]	−0.25	−2.29	8.79	−3.46	1342226902
28	ESO420-G013	041349.70−320025.3	0.0119	0.208	1.38e-15	4.0	−0.32	−2.29	8.04	−3.00	1342238379
29	3C120	043311.10+052115.6	0.0330	<0.001	3.62e-16	6.3	0.73	−2.27	8.36	−2.82	1342225795
30	ESO203-IG001[j]	044649.55−483330.6	0.0529	<0.029[k]	5.14e-17	5.1	0.06	−2.66	7.93	−3.91	1342238378
31	MCG-05-12-006	045204.96−325926.0	0.0188	0.400	3.74e-16	107	−0.59	−2.42	7.88	−3.28	1342239733
32	Ark120	051611.42−000859.4	0.0327	<0.001	1.34e-16	6.2	0.00	−2.78	7.92	−3.09	1342226750
33	VIIZw31	051646.39+794012.9	0.0539	0.491	8.55e-16	4.0	−0.33	−2.23	9.16	−2.81	1342219853
34	IRASF05187−1017	052106.53−101446.2	0.0283	0.414	2.20e-16	6.0	−0.25	−2.25	8.01	−3.26	1342227348
35	2MASXJ05580206−3820043[j]	055802.00−382004.0	0.0339	<0.001[k]	1.29e-17	3.8	> −0.44	−4.05	6.93	−4.23	1342239744
36	IRASF06076−2139	060945.74−214024.5	0.0374	0.238	1.11e-16	4.2	−0.51	−2.61	7.96	−3.67	1342230910
37	IRAS06301−7934[j]	062642.20−793630.4	0.1564	0.148	3.10e-17	3.9	−0.10	−2.39	8.69	−3.68	1342231278
38	IRAS06361−6217[j]	063635.71−622031.8	0.1596	0.052[k]	3.38e-17	3.6	−0.09	−2.80	8.75	−3.66	1342238377
39	NGC 2273	065008.72+605045.0	0.0061	0.126	7.18e-16	161	−0.44	−2.42	7.18	−2.98	1342230996
40	UGC03608	065734.41+462410.6	0.0214	0.424	1.46e-15	212	0.27	−1.64	8.46	−2.72	1342230955
41	IRASF06592−6313	065940.26−631752.4	0.0230	0.402	2.51e-16	5.5	−0.62	−2.47	7.88	−3.31	1342231286
42	Mrk0009	073657.00+584613.0	0.0399	<0.09[l]	1.12e-16	4.2	−0.50	−2.73	8.02	−3.11	1342243533
43	IRAS07598+6508[j]	080430.46+645952.9	0.1488	0.005	2.87e-17	3.9	−0.02	−3.40	8.61	−3.90	1342243534
44	Mrk0622	080741.04+390015.2	0.0232	0.245	8.36e-17	4.3	−0.63	−2.33	7.41	−3.31	1342229688

Table 1
(Continued)

No.	Name	Coordinates	z	EW[a]	f[C II][b]	S/N[c]	[C II]/11.3[d]	[C II]/7.8[e]	$L_{\rm C\,II}$[f]	$L_{\rm C\,II}/L_{\rm ir}$[g]	*Herschel* ID
		J2000		6.2 μm (μm)	(W m^{-2})		log	log	Solar log	log	
45	ESO60-IG016	085232.07−690154.8	0.0455	0.070	4.99e-16	113	0.18	−2.25	8.77	−2.95	1342228521
46	Mrk0018	090158.39+600906.0	0.0111	0.275	6.47e-16	5.1	−0.10	−1.93	7.65	−2.52	1342231958
47	MCG-01-24-012	092046.25−080322.1	0.0196	<0.005[k]	1.39e-16	5.2	0.30	−2.26	7.49	−2.87	1342231718
48	Mrk0705	092603.29+124403.6	0.0292	0.018	1.34e-16	5.1	0.00	−2.37	7.82	−2.88	1342231715
49	IRASF10038−3338	100604.65−335306.1	0.0342	<0.002[k]	4.03e-16	86	0.05	−2.89	8.44	−3.25	1342235705
50	NGC 3393	104823.39−250942.8	0.0125	<0.003	3.44e-16	70	0.73	−1.88	7.48	−2.91	1342232587
51	IRAS11119+3257	111438.88+324133.1	0.1890	0.014[k]	<2.00e-17	3.0	<−0.62	<−3.30	<8.68	<−3.94	1342232307
52	ESO319-G022	112754.18−413651.7	0.0164	0.302	4.00e-16	72	−0.05	−2.00	7.78	−3.22	1342235704
53	IRAS12018+1941[j]	120424.53+192509.8	0.1686	0.108	2.41e-17	7.9	−0.11	−2.79	8.65	−3.86	1342223403
54	UGC07064	120443.34+311038.2	0.0250	0.081	3.94e-16	4.1	0.10	−1.91	8.15	−2.89	1342223404
55	NGC 4507	123536.55−395433.3	0.0118	<0.002	5.62e-16	5.7	0.09	−2.46	7.65	−2.98	1342225720
56	PG1244+026[j]	124635.24+022208.7	0.0482	0.017	1.65e-17	3.5	−0.27	−2.80	7.35	−3.65	1342236279
57	IRAS12514+1027[j]	125400.82+101112.4	0.3182	<0.009[k]	<2.00e-17	1.6	<−0.29	<−3.00	<9.18	<−3.60	1342237582
58	ESO507-G070	130252.42−235517.8	0.0217	0.417	9.51e-16	165	0.11	−2.07	8.41	−3.03	1342225742
59	NGC 4941	130413.10−053306.0	0.0037	<0.041[k]	1.71e-16	4.9	0.32	−2.09	6.12	−3.26	1342225749
60	ESO323-G077	130626.13−402452.0	0.0156	0.029	8.27e-16	5.4	−0.17	−2.41	8.02	−2.93	1342225811
61	MCG-03-34-064	132224.45−164342.4	0.0165	<0.001[k]	1.90e-16	6.2	−0.28	−3.04	7.47	−3.65	1342225746
62	IRASF13279+3401[j]	133015.23+334629.4	0.0238	0.038[k]	2.58e-17	3.4	−0.13	−2.55	6.83	−3.63	1342232550
63	M-6-30-15	133554.54−341750.4	0.0077	<0.001	7.04e-17	4.4[h]	−0.49	−3.11	6.38	−3.53	1342225810
64	IRAS13342+3932	133624.07+391730.1	0.1793	0.073	6.54e-17	5.2	−0.20	−2.49	9.15	−3.30	1342234948
65	IRAS13352+6402[j]	133651.15+634704.7	0.2366	0.076[k]	<2.00e-17	2.4	<−0.40	<−2.80	<8.89	<−3.67	1342231427
66	IRASF13349+2438[j]	133718.73+242303.3	0.1076	<0.001[k]	2.54e-17	4.9	−0.24	−3.79	8.26	−4.04	1342236984
67	NGC 5347	135317.83+332927.0	0.0078	0.025	1.15e-16	29.0	−0.40	−2.66	6.60	−3.38	1342223133
68	IRAS14026+4341[j]	140438.72+432707.3	0.3233	0.011[k]	<2.00e-17	0.1	<−0.33	<−2.92	<9.20	<−3.71	1342236271
69	OQ+208	140700.39+282714.0	0.0766	0.018	6.28e-17	7.1	−0.43	−2.74	8.35	−3.32	1342237584
70	NGC 5548	141759.53+250812.4	0.0172	0.024	1.70e-16	4.5	−0.12	−2.48	7.45	−3.17	1342236985
71	Mrk1490	141943.27+491411.9	0.0257	0.448	3.18e-16	103	−0.60	−2.48	8.08	−3.22	1342232331
72	PG1426+015[j]	142906.59+011706.5	0.0865	<0.002	2.30e-17	3.2	−0.14	−3.06	8.02	−3.48	1342238159
73	PG1440+356	144207.46+352622.9	0.0780	0.017	5.77e-17	13.2	−0.37	−2.69	8.34	−3.19	1342223736
74	NGC 5728	144223.93−171511.0	0.0094	0.077	1.25e-15	6.4	0.07	−1.85	7.79	−2.80	1342238133
75	NGC 5793	145924.76−164136.0	0.0116	0.393	8.98e-16[i]	3.6	−0.21	−2.24	7.84	−2.79	1342238134
76	IRAS15001+1433	150231.94+142135.3	0.1627	0.140	6.40e-17	5.6	−0.32	−2.50	9.05	−3.42	1342236887
77	IRAS15225+2350[j]	152443.94+234010.2	0.1390	0.051[k]	3.23e-17	3.2	−0.17	−2.65	8.60	−3.57	1342238152
78	Mrk0876	161357.18+654309.6	0.1290	0.010	2.99e-17	3.6	−0.51	−2.98	8.50	−3.47	1342222163
79	IRASF16164−0746	161911.75−075403.0	0.0235	0.439	7.51e-16[i]	4.6	−0.11	−2.23	8.50	−3.06	1342227799
80	Mrk0883	162952.85+242638.3	0.0378	0.263	1.84e-16	5.5	−0.10	−1.83	8.18	−2.77	1342238911
81	CGCG052−037	163056.53+040458.7	0.0245	0.510	1.13e-15	233	−0.20	−2.12	8.59	−2.78	1342238909
82	IRAS16334+4630	163452.37+462453.0	0.1908	0.302	3.62e-17	4.2	−0.47	−2.44	8.95	−3.50	1342232265
83	ESO069-IG006	163811.85−682608.2	0.0464	0.497	1.08e-15[i]	3.1	−0.27	−2.27	9.14	−2.79	1342231301
84	IRASF16399−0937N	164240.11−094313.7	0.0270	0.175	1.49e-15	40	0.39	−1.62	8.80	−2.70	1342240777
85	2MASSJ165939.77+183436.9[j]	165939.77+183436.9	0.1707	0.016	<2.00e-17	2.4	<−0.30	<−2.95	<8.58	<−3.56	1342238910
86	PG1700+518	170124.91+514920.4	0.2920	<0.009	<2.00e-17	0.1	<−0.56	<−3.11	<9.10	<−3.61	1342225993
87	IRAS17044+6720[j]	170428.41+671628.5	0.1350	0.040[k]	2.06e-17	3.3	−0.39	−3.07	8.38	−3.79	1342223716
88	IRAS17068+4027	170832.12+402328.2	0.1790	<0.079[k]	3.37e-17	3.4	−0.32	−2.68	8.86	−3.54	1342232574

Table 1
(Continued)

No.	Name	Coordinates	z	EW[a]	f[C II][b]	S/N[c]	[C II]/11.3[d]	[C II]/7.8[e]	$L_{\rm C\,II}$[f]	$L_{\rm C\,II}/L_{\rm ir}$[g]	*Herschel* ID
				6.2 μm					Solar		
		J2000		(μm)	(W m^{-2})		log	log	log	log	
89	IRASF17132+5313	171420.45+531031.6	0.0509	0.420	6.09e-16[i]	3.9[h]	−0.12	−2.00	8.97	−2.91	1342223740
90	ESO138-G027	172643.35−595555.2	0.0208	0.351	1.44e-15	3.9	0.19	−1.76	8.55	−2.78	1342240168
91	CGCG141−034	175656.65+240102.0	0.0198	0.388	6.65e-16	7.8	−0.17	−2.18	8.17	−2.93	1342231759
92	H1821+643	182157.31+642036.3	0.2970	<0.002	<2.00e-17	2.5	<−0.57	<−3.37	<9.11	<−4.03	1342222100
93	IC4734	183825.75−572925.4	0.0156	0.380	1.36e-15	4.8	−0.12	−2.10	8.28	−2.99	1342241710
94	IRAS18443+7433[j]	184254.80+743621.0	0.1347	<0.051[k]	2.31e-17	3.7	−0.21	−2.92	8.43	−3.89	1342232253
95	ESO140-G043	184453.98−622153.4	0.0142	0.022	1.76e-16	45	−0.59	−2.80	7.30	−3.29	1342240169
96	1H1836−786[j]	184703.20−783151.0	0.0741	<0.012[k]	2.49e-17	3.4	−0.20	−2.75	7.92	−3.49	1342231316
97	ESO593-IG008	191431.15−211906.3	0.0487	0.405	9.51e-16[i]	3.1	0.02	−2.02	9.12	−2.76	1342231749
98	ESO-141-G055	192114.15−584013.1	0.0371	<0.003	1.32e-16	4.3	0.24	−2.54	8.02	−3.04	1342231317
99	ESO339-G011	195737.60−375608.4	0.0192	0.188	1.54e-15	5.8	0.22	−1.87	8.51	−2.62	1342232296
100	IRAS20037−1547	200631.70−153908.0	0.1919	0.043	4.63e-17	3.3	−0.32	−2.74	9.06	−3.56	1342232297
101	NGC 6860	200846.90−610601.0	0.0149	0.084	3.69e-16	6.3	0.01[l]	−2.22	7.67	−2.67	1342232295
102	ESO286-G035	210411.11−433536.1	0.0174	0.504	1.63e-15	4.7	−0.19	−2.13	8.45	−2.63	1342232563
103	NGC 7213	220916.25−471000.0	0.0058	<0.005	2.74e-16	5.3	0.03	−2.22	6.72	−3.25	1342232569
104	ESO602-G025	223125.48−190204.0	0.0250	0.300	1.24e-15	190	−0.19	−2.18	8.65	−2.69	1342233481
105	UGC12138	224017.05+080314.1	0.0250	0.081	1.43e-16	4.1	−0.43	−2.37	7.71	−3.06	1342235675
106	UGC12150	224112.21+341456.8	0.0214	0.383	8.96e-16	5.6	−0.29	−2.20	8.37	−2.95	1342223714
107	ESO239-IG002	224939.84−485058.3	0.0430	0.309	1.91e-16	6.2	−0.50	−2.44	8.31	−3.49	1342232568
108	Zw453.062	230456.55+193307.1	0.0251	0.379	1.05e-15	5.3	0.18	−1.82	8.58	−2.78	1342235676
109	IRAS23060+0505	230833.97+052129.8	0.1730	0.009[k]	<2.00e-17	3.0	<−0.48	<−3.49	<8.60	<−3.89	1342235673
110	NGC 7603	231856.62+001438.2	0.0295	0.018	2.63e-16[i]	4.2	−0.28	−2.62	8.12	−2.72	1342222576
111	MCG-83-1	234200.91−033654.4	0.0232	0.504	1.47e-15	5.8	0.09	−1.85	8.66	−2.52	1342235844
112	CGCG381−051	234841.70+021423.0	0.0307	0.542	2.34e-16	5.1	−0.24[l]	−2.13	8.10	−3.07	1342236876

Notes.

[a] Rest-frame equivalent width of 6.2 μm PAH emission feature from Sargsyan et al. (2011) used to classify source as AGN, composite, or starburst.

[b] Total flux of [C II] 158 μm emission line in units of W m^{-2} using Gaussian fit to line for simple profiles and integrated flux of line for complex profiles (noted by footnote i in this column). Line flux listed is the total flux observed within the 9 spaxels centered on the brightest spaxel, increased by a correction factor of 1.16–1.21 to include flux that would fall outside these spaxels for an unresolved source. The correction factor adopted for the range of observed [C II] wavelengths from 160 μm to 210 μm is $1.16(\lambda/158\,\mu{\rm m})^{0.17}$. Uncertainties of individual fits given by S/N in the next column; systematic uncertainty for all fluxes depends on PACS flux calibration, estimated as ±12% in the PACS Spectroscopy performance and calibration document PICC-KL-TN-041.

[c] Signal-to-noise ratio of total line flux in brightest spaxel, using 1σ uncertainty of profile fit.

[d] Ratio of flux in [C II] 158 μm to flux of PAH 11.3 μm emission feature, from Sargsyan et al. (2011).

[e] Ratio f([C II])/νf_ν(7.8 μm) using f_ν(7.8 μm) from Sargsyan et al. (2011).

[f] [C II] 158 μm emission line luminosity in $L_\odot$using luminosity distances determined for H_0 = 71 km s^{-1} Mpc^{-1}, Ω_M = 0.27, and Ω_Λ = 0.73, from Wright (2006): http://www.astro.ucla.edu/wright/CosmoCalc.html [$\log L_{\rm C\,II}$ (solar) = $\log L_{\rm C\,II}$ (W) − 26.59].

[g] Ratio of [C II] luminosity to $L_{\rm ir}$ using $L_{\rm ir}$ given in Sargsyan et al. (2011) from $f_{\rm ir}$ determined as in Sanders & Mirabel (1996), $f_{\rm ir} = 1.8 \times 10^{-11}[13.48 f_\nu(12) + 5.16 f_\nu(25) + 2.58 f_\nu(60) + f_\nu(100)]$ in erg cm^{-2} s^{-1} using *IRAS* flux densities at 12 μm, 25 μm, 60 μm, and 100 μm.

[h] Brightest spaxel displaced one spaxel from central 3,3 spaxel.

[i] [C II] line profile is asymmetric or has component structure so total line flux is integrated flux including all components rather than flux within a single Gaussian fit.

[j] Observation made with two repetition cycles of line spectroscopy point-source chop nod mode; all observations without note made with single cycle.

[k] IRS spectrum shows 9.7 μm silicate feature in absorption.

[l] For these four sources, spectra are not in CASSIS because IRS spectra obtained in mapping mode; PAH measures from Wu et al. (2009).

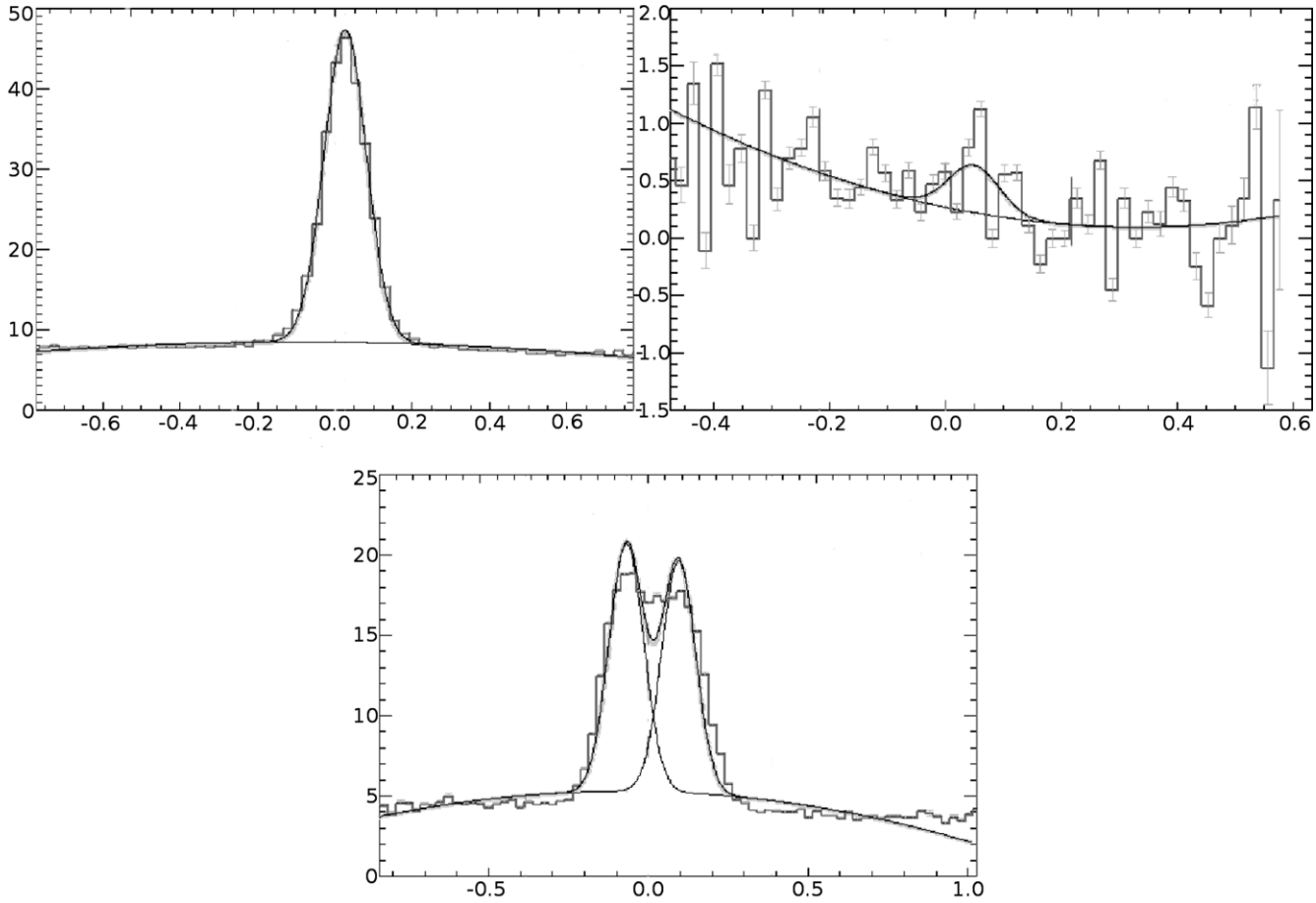

Figure 3. Examples of line fits in the brightest spaxel for three sources in Table 1. Vertical axes are flux density in Jy; horizontal axes are wavelength differences in μm from [C II] rest wavelengths derived using redshifts in Table 1. Upper left panel (source 28 in Table 1) is a high S/N detection for which the line flux derives from the Gaussian fit shown; upper right panel (source 92 in Table 1) is an upper limit; lower panel (source 83) is a complex, broad profile for which the line flux is the total integrated flux within the wavelength bounds of the two profiles shown. [C II] line fluxes in Table 1 are the sum of the brightest spaxel plus the 8 surrounding spaxels, increased by a correction factor of 1.16–1.21 (depending on redshift) to include the flux from an unresolved source that would fall outside these 9 spaxels.

of 28″ by 28″. Calibration communicated to us by the PACS calibration team gives the result that the $f(3 \times 3)$ should be corrected by a factor 1.16 to give the total flux at 160 μm for an unresolved source that is precisely centered. This correction is slightly wavelength dependent, increasing to a maximum correction of 1.21 for our highest redshift source, for which the [C II] line is observed at 212 μm.

To list the total fluxes of detected sources, therefore, we correct $f(3 \times 3)$ to include flux outside these spaxels by taking values between $1.16 f(3 \times 3)$ and $1.21 f(3 \times 3)$ as the total source line flux, depending on the observed frame wavelength according to the formula given in the footnote to Table 1. These corrected $f(3 \times 3)$ are the values listed in Table 1 for the total [C II] line flux.

These two alternative measures of total line fluxes from the brightest spaxel and from $f(3 \times 3)$ are compared in Figure 4. This comparison illustrates empirically the large error that can arise from imperfect centering if using only the brightest spaxel. The plot compares the single brightest spaxel corrected by a factor of 1.95 with the sum of the 9 spaxels corrected by 1.16. The limiting ratio for these corrected fluxes should be unity ($\log = 0$ on vertical axis) for a perfectly centered point source, and several sources satisfy this value. Small centering uncertainties have little effect within the large area of the $f(3 \times 3)$ flux, so the scatter in $1.16 f(3 \times 3)/1.95 f$(brightest) primarily demonstrates the uncertainty arising when using only the brightest spaxel to determine total flux. The vertical dispersion of the points and the dominance of values above unity can be explained by slight differences in source centering within the brightest spaxel. (To simplify this illustrative calculation, we apply no wavelength dependence for different redshifts to the correction factors for Figure 4 because such differences are small compared to the centering uncertainties.)

For example, in the extreme case of a source being offset 5″ in a direction such that the centering is on a spaxel corner, the "brightest spaxel" would be shared evenly among 4 spaxels. In this extreme example, the brightest spaxel would have 1/4 of the flux within the 4 spaxels, or within encircled energy of radius 10″ (taken as 72% of the total flux for an unresolved source), so the brightest spaxel has 18% of the total source flux. For this extreme case of sharing the brightest spaxel among 4 spaxels, therefore, the correction to total flux derived only from the brightest spaxel should actually be a factor of 5.6 and not a factor of 1.95, so the corrected total flux from the brightest spaxel alone if corrected by 1.95f(brightest) would be erroneously faint by a factor of 2.9. This extreme case is shown as the upper line in Figure 4. Intermediate centering of an unresolved source within the brightest spaxel would lead to values anywhere between the upper and lower lines in Figure 4, so centering uncertainties alone of $<\pm 5''$ could explain the dispersion of all points in Figure 4, except for the one source falling above the upper line.

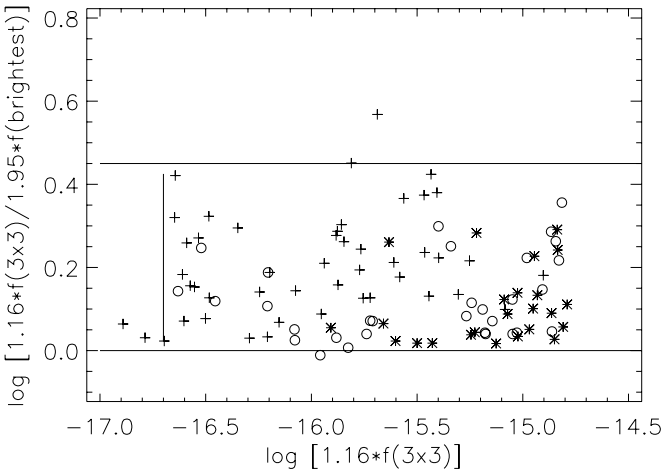

Figure 4. Vertical axis compares total corrected [C II] source flux derived from observed flux in 3 × 3 spaxels compared to corrected flux derived only from the brightest spaxel; both observed measures are corrected for fractional flux that would fall outside of those spaxels for a perfectly centered, unresolved source, using corrections of 1.95*f*(brightest) and $1.16\,f(3\times3)$ at 158 μm (small changes in corrections because of different redshifts are ignored in this ratio comparison). Horizontal axis is corrected total [C II] flux $1.16\,f(3\times3)$ in W m^{-2}. The 102 detected sources in Table 1 are shown as crosses for AGNs, open circles for composite AGNs plus starbursts, and asterisks for starbursts (all using the EW (6.2 μm) classification discussed in Section 2.1). Vertical line defines flux upper limit for the 10 undetected sources in Table 1. Upper horizontal line is the maximum value of ratio $1.16\,f(3\times3)/1.95f$(brightest) that can arise for an unresolved source because of imperfect centering; sources above this line must be extended. Lower horizontal line is ratio of unity expected for a perfectly centered unresolved source.

Extended sources would also have ratios above unity in Figure 4, and it is not possible to determine from this ratio alone whether a source is unresolved but not perfectly centered, or whether the source is slightly extended. A diffuse source so extended that it evenly fills the central 3 × 3 spaxels (so each of these 9 spaxels has the same flux as the brightest spaxel) would have $\log[1.16\,f(3\times3)/1.95f(\text{brightest})] = 0.73$, but no sources show this extreme ratio. This is proof that no sources are extended as large as 30″.

Further evidence that most sources are unresolved is the similar distribution in ratio $1.16\,f(3\times3)/1.95f$(brightest) between starbursts and AGNs. If some sources are extended, they should be extended starbursts instead of unresolved AGNs, but starbursts show no more extension to large ratios than do the AGN. The consequence to our analysis of having some marginally resolved sources would be that the total [C II] flux is erroneously large compared to PAH, because the PAH measure derives from IRS measures calibrated for unresolved sources. When comparing the [C II]/PAH ratio below in Section 3.2, however, the only three sources with [C II]/PAH ratios significantly above the dispersion are three AGNs, and none of these three show any evidence of spatial extent in the PACS images.

Figure 4 also illustrates how upper limits for non detections are determined. The detection limit for our sample is at $\log f$([C II] 158 μm) ~ -16.7 in units of W m^{-2}. This value is taken as the upper limit of [C II] line flux for the 10 sources which are not detected, according to our criterion of S/N < 3 in the brightest spaxel.

3. ANALYSIS AND RESULTS

In the present analysis, the mid-infrared spectroscopic features used for comparisons to [C II] line luminosities are the PAH emission features at 6.2 μm and 11.3 μm. These values are tabulated by Sargsyan et al. (2011) measured as described above in Section 2.1. The 11.3 μm PAH is used as the PAH flux measurement for comparison with [C II] because this feature is detected in all but two of our sources, whereas the 6.2 μm feature is only a limit in 25 sources. The EW (6.2 μm) is used only for source classification, and all sources with limits for EW (6.2 μm) have classification as AGN because of the weak 6.2 μm PAH.

3.1. Comparison of PAH and [C II]

Photoionization and photoelectric heating models for [C II] (Stacey et al. 1991; Hollenbach & Tielens 1999; Malhotra et al. 2001; Abel et al. 2009) in comparison with previously available observations (Luhman et al. 2003; Gracia-Carpio et al. 2011; Stacey et al. 2010) indicate that [C II] emission arises primarily in PDRs, with ionization produced by the hot stars of the adjacent H II region. Although [C II] can arise in any region with singly ionized carbon and sufficiently energetic electrons for collisional excitation, the level of ionization seems the most important parameter for line strength; models show a weakening of [C II] if the ionization parameter increases, resulting in a diminishing of the PDR compared to the H II region. This could be the result of harder ionization either from AGNs or from unusually hot stars in compact, young starbursts.

Comparisons of 6.2 μm PAH and [C II] using *ISO* results showed overall consistency between the two measures of PDRs but discussed various reasons why detailed agreement is not expected (Helou et al. 2001; Luhman et al. 2003). Models as well as *Herschel* observations of spatially resolved [C II] emission regions and Galactic PDRs show that detailed relations are complex (Mookerjea et al. 2011; Lebouteiller et al. 2012; Velusamy et al. 2012; Bernard-Salas et al. 2012) but generally confirm that [C II] emission arises primarily in the PDR and scales with the PAH (Croxall et al. 2012).

For our sample, the objective is an empirical observational comparison to determine how the observed [C II] and PAH fluxes scale together when integrated over many star-forming regions throughout many sources. Such scaling would be an indication that the [C II] luminosity can be used as a quantitative measure of PDRs and SFRs in the same fashion as the PAH luminosity can be used (Peeters et al. 2004) and thereby allow reliable use of [C II] as a star formation indicator. The large sample of sources enabled by the new *Herschel* observations can also determine the cosmic dispersion in this comparison and the extent to which the differences in [C II]/PAH ratios seen on small scales within starburst galaxies (e.g., Beirão et al. 2012) average out when integrated over entire starburst systems.

Figure 5 compares the [C II] total line flux, f([C II] 158 μm), with the 11.3 μm PAH feature, f(11.3 μm PAH), as a function of the source classification from EW (6.2 μm). Figure 6 shows the [C II]/PAH ratio compared to total infrared luminosity $L_{\rm ir}$. (For comparison, the ground-based measurement of [C II] for the source at $z = 1.3$ from Hailey-Dunsheath et al. 2010 is also shown in Figure 5 because this source has an IRS spectrum allowing PAH measurement; this source has a higher redshift than any of our PACS sources.) Also shown for comparison in these and subsequent figures is the prototype local ULIRG Markarian 231 using [C II] fluxes from Fischer et al. (2010) and PAH measures from Sargsyan et al. (2011), because this source satisfies our selection criteria.

Figure 5 shows the important conclusion that the [C II] to PAH ratio is independent of starburst/AGN classification. The median ratios for all classes are the same. Figure 6 shows that the

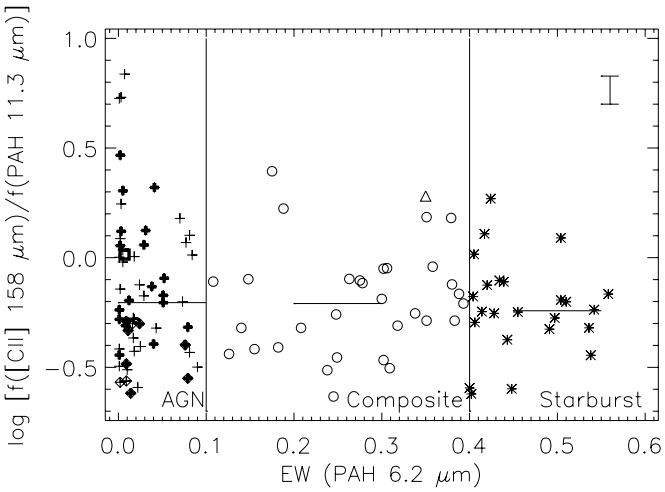

Figure 5. Ratio of [C II] to PAH 11.3 μm line fluxes, compared to source classification from EW (PAH 6.2 μm) measured in μm. Crosses are AGNs from the EW classification (discussed in Section 2.1); thick crosses are those sources with silicate absorption in IRS spectra noted in Sargsyan et al. (2011). Open circles are composite AGNs plus starbursts, and asterisks are starbursts. Sources with diamonds (all AGNs) are upper limits to [C II] line fluxes in Table 1. Triangle is the source at $z = 1.3$ from Hailey-Dunsheath et al. (2010). Square is Markarian 231 using [C II] flux from Fischer et al. (2010). Horizontal bars are medians within each category; medians include limits because all limits fall below the median. Vertical error bar shows the observational uncertainty for individual points assuming flux uncertainties of $\pm$12% for f([C II]) and $\pm$10% for f(PAH 11.3 μm).

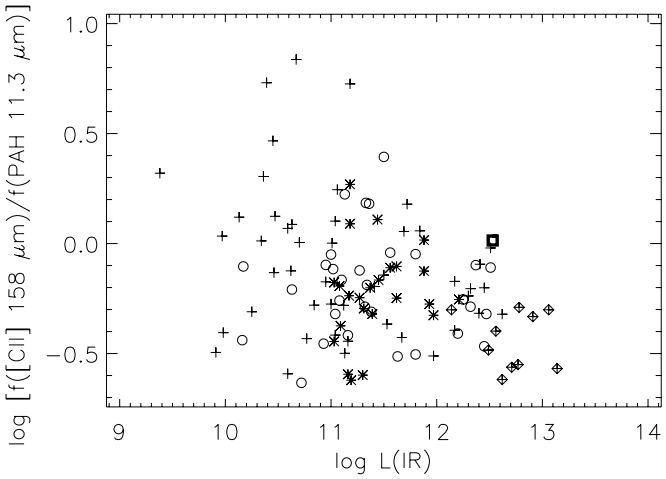

Figure 6. Ratio of [C II] and PAH 11.3 μm line fluxes, compared to total infrared luminosity L_{ir} in $L_{\odot}$. Crosses are AGNs from the EW classification, open circles are composite AGNs plus starbursts, and asterisks are starbursts. Sources with diamonds (all AGNs) are upper limits to [C II] line fluxes in Table 1. Square is Markarian 231.

ratio does not depend on source luminosity. The overall median and dispersion for all sources is $\log [f([\mathrm{C\,II}]\ 158\ \mu\mathrm{m})/f(11.3\ \mu\mathrm{m}\ \mathrm{PAH})] = -0.22 \pm 0.25$. This scatter is a measure of the cosmic dispersion in the comparison of [C II] and PAH when integrated fluxes that include entire, unresolved collections of starbursts are observed. This dispersion is independent of AGN/starburst classification which implies that the dispersion is a measure of variances within the starbursts.

Because the PAH luminosity is determined by the starburst, this result means that the [C II] line flux also depends only on the starburst component of the source, regardless of the fractional starburst/AGN mix. This result indicates that [C II] luminosity can be used as a measure of starburst luminosity with as much reliability as PAH, because [C II] is a measure of the same PDRs as is the mid-infrared PAH. The [C II] luminosity measures SFR in any source for which [C II] is observed, even if the source luminosity is dominated by an AGN.

A question about the use of the 11.3 μm PAH feature for flux measures is whether this feature might be affected by silicate extinction in sources showing strong silicate absorption as in Figure 1, because the PAH feature falls within the broad silicate absorption centered at 9.7 μm. The silicate absorption is always associated with AGN classification and is attributed to thick dust clouds close to the AGN (e.g., Imanishi et al. 2007; Levenson et al. 2007). An important question about the geometry of these absorbing clouds is whether they also surround the starburst regions. The [C II] results allow a test of this. If the starbursts are affected by the same silicate absorption that affects the AGN, then the f([C II] 158 μm)/f(11.3 μm PAH) ratio should be systematically larger in sources with silicate absorption because the [C II] is not affected by the silicate absorption feature.

These absorbed sources are noted in Table 1 and shown in Figure 5, where it is seen that there is no systematic difference in the ratio for the absorbed AGNs compared to the emission AGN. Formally, the median for the absorbed AGNs is $\log [f([\mathrm{C\,II}]\ 158\ \mu\mathrm{m})/f(11.3\ \mu\mathrm{m}\ \mathrm{PAH})] = -0.23$ and is -0.18 for the emission AGNs, which is opposite to what would arise if the absorbed AGNs have suppressed 11.3 μm PAH. (The AGN median shown in the figure is for all AGNs.) Based on this observation, we conclude that the 11.3 μm PAH feature arises outside of the region affected by silicate absorption, so this feature has the same reliability for measuring starburst PDRs regardless of the presence of silicate absorption.

Among all of the sources in Figures 5 and 6, only three appear anomalous. These are all AGNs and have the largest f([C II])/f(PAH) ratios—sources 3C 120, Mrk 590, and NGC 3393 in Table 1—with f([C II])/f(PAH) about a factor of 10 greater than the median. All have strong and reliable [C II] detections with no unusual profiles or evidence of spatial mismatches or source extension. The PAH 11.3 μm feature is weak in all three, but independent CASSIS spectra yield fluxes consistent to within $\sim$30%, so there is no indication that the anomalous weakness of PAH is a measurement error. All are silicate emission sources, so the anomalies cannot be explained by silicate absorption associated with the AGN. These are the only sources among the 112 sources in all categories with excess [C II] luminosity compared to PAH. Why are the ratios so unusual in these three sources?

There are various possible explanations. One possibility is that an unusual combination of radiation hardness and ionization parameter, caused by geometry, density distributions, or ionizing spectrum, causes PAH emission in the PDR to be suppressed while maintaining [C II] within the H II region (Luhman et al. 2003). An alternative possibility could be that the PAHs are weak because of star formation taking place in dense clouds which are so obscured that the mid-infrared PAH from the starburst PDR suffers significant extinction compared to the far-infrared [C II]. Because the AGN is not absorbed, such clouds would require a small filling factor or geometric placement outside of the observer's line of sight to the AGN. In this circumstance, we would expect mid-infrared emission lines associated with any obscured starburst, such as [Ne II] 12.8 μm, also to be unusually weak compared to [C II], and would also expect to observe excess far-infrared continuum from the obscured starbursts. We defer further analysis of this question until more comparisons

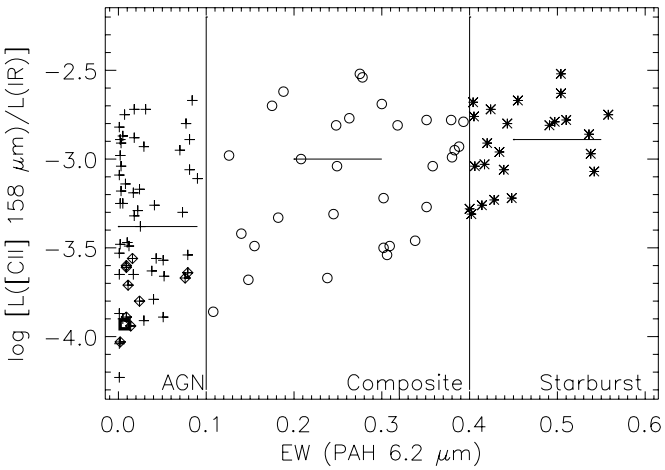

Figure 7. Ratio of [C II] luminosity L([C II]) to total infrared luminosity $L_{\rm ir}$, compared to source classification from EW (PAH 6.2 μm) measured in μm. Crosses are AGNs from the EW classification, open circles are composite AGNs plus starbursts, and asterisks are starbursts. Sources with diamonds (all AGNs) are upper limits to [C II] line fluxes in Table 1. Square is Markarian 231. Horizontal bars are medians within each category; medians include limits because all limits fall below the median. Median for starbursts is used in the text to calibrate L([C II]) compared to star formation rate, giving $\log {\rm SFR} = \log L([{\rm C\,II}]) - 7.08 \pm 0.3$, for SFR in $M_\odot$ yr^{-1} and L([C II]) in $L_\odot$.

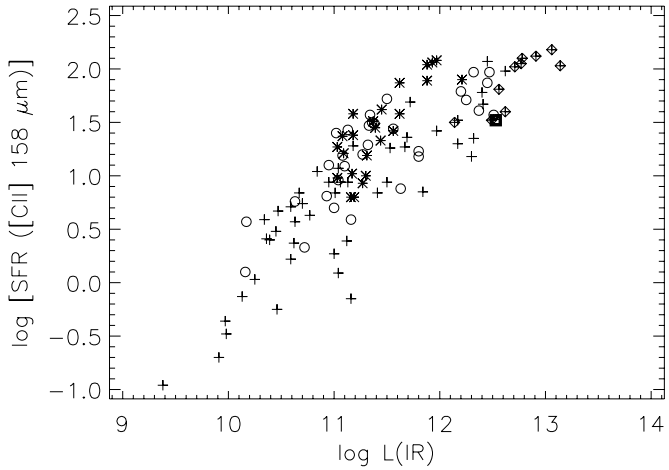

Figure 8. Star formation rate in all sources in $M_\odot$ yr^{-1} measured using L([C II]) to SFR calibration from Figure 7. Crosses are AGNs from the EW classification, open circles are composite AGNs plus starbursts, and asterisks are starbursts. Sources with diamonds (all AGNs) are upper limits to SFR from upper limits to [C II] line fluxes in Table 1. Square is Markarian 231. $L_{\rm ir}$ is in $L_\odot$.

are made among *Spitzer* mid-infrared emission lines, [C II], and SEDs for our full sample of sources.

3.2. Star Formation Rate from [C II]

For eventual application to high-redshift, dusty sources in which [C II] measurements with ALMA or other submillimeter/millimeter spectroscopy are the primary diagnostic, calibration of [C II] luminosity to SFR is our most important objective. The conclusion reached above, that [C II] luminosity L([C II]) measures the PDRs arising from star formation, encourages the calibration of SFR compared to L([C II]).

Determining the SFR for dusty sources ultimately traces back to the method of Kennicutt (1998), in which the total infrared luminosity $L_{\rm ir}$ is attributed to reradiation by dust of the primary stellar luminosity from the starbursts. The original calibration is $\log {\rm SFR} = \log L_{\rm ir} - 9.76$, for $L_{\rm ir}$ in $L_\odot$. We adopt the updated calibration in Buat et al. (2010), giving $\log {\rm SFR} = \log L_{\rm ir} - 9.97$. All of our sources have $L_{\rm ir}$ listed in Sargsyan et al. (2011) determined using the formulation in Sanders & Mirabel (1996), described in the footnote to Table 1. This $L_{\rm ir}$ is an estimate of the complete 8 μm to 1000 μm luminosity derived from all four *IRAS* bands.

By comparing $L_{\rm ir}$ to L([C II]) for starbursts, a calibration can be determined between L([C II]) and SFR. It is necessary to assure that $L_{\rm ir}$ arises only from a starburst and is not contaminated by an AGN component. Figure 7 compares the ratio $L([{\rm C\,II}])/L_{\rm ir}$ depending on source classification. The medians seen in this figure trend as expected if L([C II]) measures only the starburst component but $L_{\rm ir}$ arises from both starburst and AGN components. As the contribution to $L_{\rm ir}$ arising from AGN luminosity increases compared to the L([C II]) arising from starburst luminosity, the ratio $L([{\rm C\,II}])/L_{\rm ir}$ systematically decreases for AGNs (this is discussed further in Section 3.3 in context of the C II deficit). To calibrate SFR to L([C II]) using $L_{\rm ir}$, AGNs and composites in Figure 7 are not used because some fraction of the $L_{\rm ir}$ arises from AGNs.

For starbursts only in Figure 7, the observed median ratio $\log L([{\rm C\,II}])/L_{\rm ir} = -2.89$. This gives the calibration $\log {\rm SFR} = \log L([{\rm C\,II}]) - 7.08 \pm 0.3$, for SFR in $M_\odot$ yr^{-1} and L([C II]) in $L_\odot$. The uncertainty arises from the 1σ dispersion among the starburst points shown in Figure 7. This result is our SFR calibration. Taken with the conclusions from Figures 5 and 6, that L([C II]) scales with the starburst component in all sources, this calibration can be applied to any source in which [C II] is measured.

The resulting measures of SFR are shown in Figure 8. The results show that the greatest SFRs are in sources with a starburst classification from EW (6.2 μm) even though these sources do not have the most luminous $L_{\rm ir}$. For example, among sources with $\log {\rm SFR} > 1.8$, six are starbursts, three are composites, and only two are AGNs (not counting upper limits). This preponderance of starbursts is even greater when compared to the sample sizes; this high SFR includes 6 of 24 starbursts, 3 of 31 composites, and only 2 of 55 AGNs. The dominance in SFR by starbursts arises despite the fact that the largest $L_{\rm ir}$ ($L_{\rm ir} > 10^{12}$ $L_\odot$) are dominated by AGNs. The maximum SFR in this sample is $\sim$100 $M_\odot$ yr^{-1}, about a factor of 10 less than in the most luminous starbursts at $z \sim 2$ with SFR measured using PAH luminosity (Weedman & Houck 2008).

Another important result from Figure 8 is that AGNs are generally accompanied by starbursts, but AGN sources (including composites) encompass a much larger range and dispersion of SFR than do the pure starbursts. AGNs have $-1 < \log {\rm SFR} < 2$ compared to $0.8 < \log {\rm SFR} < 2.0$ for starbursts. At luminosity $L_{\rm ir} \sim 10^{11}$ $L_\odot$, AGNs have $-0.2 < \log {\rm SFR} < 1.3$ compared to $0.7 < \log {\rm SFR} < 1.7$ for starbursts. Composites are intermediate. These results mean that some fraction of $L_{\rm ir}$ arises from an accompanying starburst even for AGN-dominated $L_{\rm ir}$, but the large dispersion in SFR/$L_{\rm ir}$ for AGN means this fraction varies by a factor of more than 10.

3.3. The [C II] "Deficit" and Source Classification

A primary result from analysis of [C II] luminosity from *ISO* measures was the discovery of the "[C II] deficit," whereby the most luminous sources have weak L([C II]) compared to infrared luminosity (Luhman et al. 2003; Helou et al. 2001). This is confirmed in new *Herschel* results (Gracia-Carpio et al. 2011) and ground-based results (Stacey et al. 2010). The explanation of this deficit remains a question, and there are many possibilities,

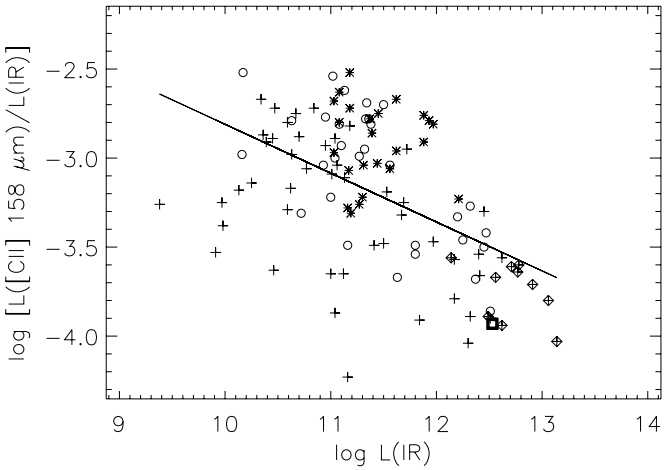

Figure 9. Ratio of [C II] luminosity to total infrared luminosity, L_{ir}, compared to L_{ir} in $L_{\odot}$. Crosses are AGNs from the EW (PAH 6.2 μm) classification, open circles are composite AGNs plus starbursts, asterisks are starbursts, and sources with diamonds (all AGNs) are upper limits to [C II] line fluxes in Table 1; line is linear fit to all of these points. Square is Markarian 231.

thoroughly reviewed by Luhman et al. (2003). These include H II regions with densities above the critical density for [C II] emission, regions with increasing ionization parameter and harder ionizing radiation which diminishes or destroys the PDR (Malhotra et al. 2001; Abel et al. 2009; Stacey et al. 2010; Gracia-Carpio et al. 2011), and self-absorption or dust extinction of [C II].

One simple possibility to explain the deficit is that the most luminous sources are powered primarily by AGNs so that most of the infrared luminosity arises from AGNs which do not have accompanying L([C II]) from a starburst PDR. In this case, there would be no difference within the starburst regions or PDRs between ULIRGs and lower luminosity starbursts; the deficit is simply a consequence of increased AGN activity and the subsequent additional L_{ir}. This would be an important conclusion because of previous suggestions that individual starbursts in ULIRGs have higher luminosity density than other starbursts (Luhman et al. 2003; Stacey et al. 2010).

Because we have already concluded that L([C II]) scales with the starburst component, we would expect [C II] to be relatively weaker if an AGN dominates L_{ir} than if L_{ir} arises primarily from starbursts. This is already shown in Figure 7, which demonstrates that AGNs systematically have smaller values of $L([C\,II])/L_{ir}$. Whether AGNs are responsible for the deficit is tested in Figure 9 by comparing $L([C\,II])/L_{ir}$ with L_{ir} using the source classifications derived from EW (6.2 μm). The overall distribution of points in Figure 9 demonstrates a deficit similar to the results summarized in Gracia-Carpio et al. (2011) and Stacey et al. (2010). The line is fit to all points in our sample and would have an even steeper slope depending on the actual values for the upper limits.

Figure 9 indicates that the [C II] deficit shown by our sample arises because of AGNs. All sources with a deficit, $\log L([C\,II])/L_{ir} < -3.4$, are either AGNs or composites. All AGNs do not show deficits, however. Some lower luminosity AGNs have $L([C\,II])/L_{ir}$ ratios similar to starbursts; the deficit arises only in the highest luminosity AGNs. The ratios in Figure 9 and the SFRs shown in Figure 8 indicate that the starbursts within our sample have a maximum luminosity $L_{ir} \sim 10^{12}\ L_{\odot}$ at which $\log L([C\,II])/L_{ir} \sim -3.4$. Any further increase in L_{ir} comes only from an AGN component without additional L([C II]), thereby decreasing $L([C\,II])/L_{ir}$.

These conclusions consider only the total infrared luminosity L_{ir} and do not address the important question of how the shape of the continuum SED depends on the AGN/starburst fraction. A measure of "far-infrared luminosity" is also defined by Sanders & Mirabel (1996) using L_{fir} as an estimate of the 40 μm to 120 μm luminosity derived only from the 60 μm and 100 μm bands, and L_{fir} is used as a luminosity measure in some of the other analyses cited above. Our PACS results also provide the far-infrared continuum flux density at rest-frame 158 μm, and we will discuss these results in a future analysis to determine, for example, if sources with larger starburst fractions determined from L([C II]) also have a greater proportion of far-infrared luminosity.

3.4. Comparisons to Dusty Sources at $z \sim 2$

At redshifts $z \sim 2$, the rest-frame spectral features observed with the *Spitzer* IRS are those shown in Figure 1. For starbursts and dusty, absorbed AGNs, the spectra show a maximum near 7.8 μm. For starbursts, this is the peak of the PAH feature. For absorbed AGNs, this is a localized continuum maximum between absorptions on both sides of the maximum (Spoon et al. 2004). These heavily absorbed AGNs are the AGN among the DOGs and were generally not known from optical observations because of the heavy extinction by dust. Type 1 AGNs or optically discovered quasars are also luminous in the infrared but have silicate in emission (e.g., Hao et al. 2005), which does not show the localized peak at 7.8 μm.

The presence of the 7.8 μm maximum explains why large numbers of dusty, optically obscured *Spitzer* sources are selected at $z \sim 2$, because this maximum becomes centered within the broadband 24 μm filter used for surveys with the Multiband Imaging Photometer for *Spitzer* (Rieke et al. 2004). *Spitzer*-discovered sources at these redshifts have also been measured in far-infrared, submillimeter, and millimeter wavelengths and compared to the *Herschel* or submillimeter-discovered populations (Magdis et al. 2010; Kovacs et al. 2010; Lonsdale et al. 2010). (The highest redshift source confidently discovered based on IRS spectra has $z = 3.35$, a redshift limit set by the observable IRS long wavelength limit for identifying the 7.8 μm maximum.)

In spectra of faint sources with poor S/N, the spectral maximum near 7.8 μm is the most reliable observational measure of mid-infrared (rest-frame) flux density and can be easily measured from published spectra of faint, high-redshift sources (e.g., Sajina et al. 2007; Farrah et al. 2008; Desai et al. 2009; Coppin et al. 2010). For these reasons, our previous analyses of starbursts and AGNs observed with the IRS use the parameter $\nu L_{\nu}(7.8\,\mu m)$ as a measure of infrared luminosity for local sources and *Spitzer*-discovered DOGs at $z \gtrsim 2$ (e.g., Houck et al. 2007; Weedman & Houck 2009b; Sargsyan et al. 2010).

Future detections or limits on [C II] at high redshifts will provide important constraints on the earliest epochs of formation for luminous dusty starbursts and AGNs. It is useful, therefore, to compare $f_{\nu}(7.8\,\mu m)$ and [C II] line fluxes for our present sample to predict [C II] line fluxes for the dusty population at $z > 2$, when scaled from the DOGs already known at $z \sim 2$.

The comparison is shown in Figure 10, using the maximum flux densities $f_{\nu}(7.8\,\mu m)$ from Sargsyan et al. (2011) and comparing $f([C\,II])/\nu f_{\nu}(7.8\,\mu m)$ so that units are the same. If high-redshift populations have the same [C II] characteristics as our low-redshift *Herschel* sample, these results

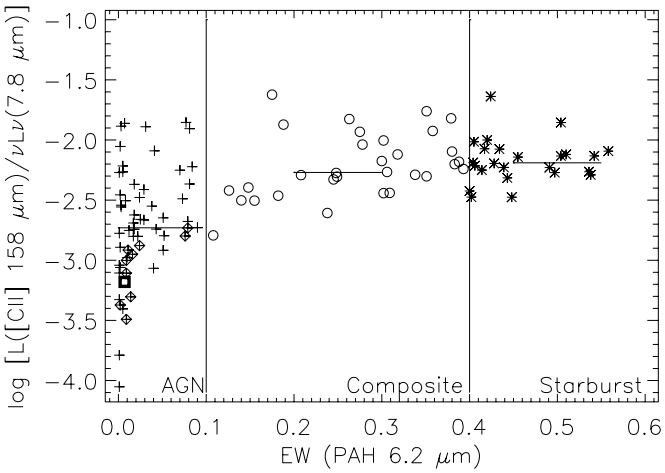

Figure 10. Ratio of luminosities $L([\mathrm{C\,II}])/\nu L_\nu(7.8\,\mu\mathrm{m})$ for all sources in Table 1. Symbols are as in preceding figures. Horizontal bars are medians within each category; medians include limits because all limits fall below the median.

predict $\log[f([\mathrm{C\,II}])/\nu f_\nu(7.8\,\mu\mathrm{m})] = -2.2 \pm 0.2$ for starbursts and $\log[f([\mathrm{C\,II}])/\nu f_\nu(7.8\,\mu\mathrm{m})] = -2.7 \pm 0.5$ for AGNs. The larger dispersion of this ratio for AGNs arises because of the large range in the starburst component of AGNs, discussed in Section 3.2.

4. CONCLUSIONS AND SUMMARY

The *Herschel* PACS instrument has been used to observe [C II] 158 μm line fluxes in 112 sources having a wide range of starburst and AGN classifications chosen because they have complete mid-infrared spectra with the *Spitzer* IRS and have complete *IRAS* fluxes for determining L_{ir}. Of the 112 sources, 102 have reliable line detections and 10 are upper limits.

It is found that the [C II] line flux correlates with the flux of the 11.3 μm PAH feature, $\log[f([\mathrm{C\,II}]\ 158\,\mu\mathrm{m})/f(11.3\,\mu\mathrm{m\ PAH})] = -0.22 \pm 0.25$. This $f([\mathrm{C\,II}])/f(\mathrm{PAH})$ ratio is independent of AGN/starburst classification as determined from EW of the 6.2 μm PAH feature. We conclude that [C II] line flux measures the starburst component of any source as reliably as the PAH feature.

This conclusion leads to a calibration of SFR determined from the luminosity of [C II] for the starburst component in any source. The calibration is derived using L_{ir} only for starbursts to avoid AGN contamination of L_{ir} and has the result $\log \mathrm{SFR} = \log L([\mathrm{C\,II}]) - 7.08 \pm 0.3$, for SFR in $M_\odot\ \mathrm{yr}^{-1}$ and $L([\mathrm{C\,II}])$ in $L_\odot$. This result applies to the starburst component of any source in which [C II] is observed. The maximum SFRs in the sample are 100 $M_\odot\ \mathrm{yr}^{-1}$, and SFRs are dominated by sources classified as starbursts, but most AGNs also have some measurable starburst component.

The [C II] "deficit," or a smaller ratio of $L([\mathrm{C\,II}])/L_{\mathrm{ir}}$ with increasing L_{ir}, is shown to arise because L_{ir} of the most luminous sources arises primarily from an AGN so that $L([\mathrm{C\,II}])$ from the starburst component is small in comparison.

We thank those who developed the *Herschel* Observatory for the opportunity to observe with open time. PACS has been developed by a consortium of institutes led by MPE (Germany) and including UVIE (Austria); KU Leuven, CSL, IMEC (Belgium); CEA, LAM (France); MPIA (Germany), INAF-IFSI/OAA/OAP/OAT, LENS, SISSA (Italy); and IAC (Spain). This development was supported by the funding agencies BMVIT (Austria), ESA-PRODEX (Belgium), CEA/CNES (France), DLR (Germany), ASI/INAF (Italy), and CICYT/MCYT (Spain). Support for this work by the IRS GTO team and *Herschel* observing team at Cornell University was provided by NASA through Contracts issued by JPL/Caltech and by the NASA Herschel Science Center. L.S. also acknowledges support from the Deutsche Forschungsgemeinschaft grant En 176/36-1. J.B.S. acknowledges support from a Marie Curie Intra-European Fellowship within the 7th European Community Framework Program under project number 272820.

REFERENCES

Abel, N. P., Dudley, C., Fischer, J., Satyapal, S., & van Hoof, P. A. M. 2009, ApJ, 701, 1147
Alexander, D. M., Bauer, F. E., Chapman, S. C., et al. 2005, ApJ, 632, 736
Beirão, P., Armus, L., Helou, G., et al. 2012, ApJ, 751, 144
Bernard-Salas, J., Habart, E., Arab, H., et al. 2012, A&A, 538, 37
Brandl, B., Bernard-Salas, J., Spoon, H. W. W., et al. 2006, ApJ, 653, 1129
Brauher, J. R., Dale, D. A., & Helou, G. 2008, ApJS, 178, 280
Brown, M., Brand, K., Dey, A., et al. 2006, ApJ, 638, 88
Buat, V., Giovannoli, E., Burgarella, D., et al. 2010, MNRAS, 409, 1
Chapman, S., Blain, A., Smail, I., & Ivison, R. 2005, ApJ, 622, 77
Chary, R., & Elbaz, D. 2001, ApJ, 556, 562
Coppin, K., Pope, A., Menndez-Delmestre, K., et al. 2010, ApJ, 713, 503
Croom, S. M., Smith, R. J., Boyle, B. J., et al. 2004, MNRAS, 349, 1397
Croxall, K. V., Smith, J. D., Wolfire, M. G., et al. 2012, ApJ, 747, 81
Desai, V., Soifer, B. T., Dey, A., et al. 2009, ApJ, 700, 1190
Dey, A., Soifer, B. T., Desai, V., et al. 2008, ApJ, 677, 943
Fan, X., Hennawi, J. F., Richards, G. T., et al. 2004, AJ, 128, 515
Farrah, D., Lonsdale, C. J., Weedman, D. W., et al. 2008, ApJ, 677, 957
Fischer, J., Sturm, E., Gonzlez-Alfonso, E., et al. 2010, A&A, 518, 41
Genzel, R., Lutz, D., Sturm, E., et al. 1998, ApJ, 498, 579
Gracia-Carpio, J., Sturm, E., Hailey-Dunsheath, S., et al. 2011, ApJ, 728, 7
Hailey-Dunsheath, S., Nikola, T., Stacey, G. J., et al. 2010, ApJ, 714, 162
Hao, L., Spoon, H. W. W., Sloan, G. C., et al. 2005, ApJ, 625, L75
Helou, G., Malhotra, S., Hollenbach, D. J., Dale, D. A., & Contursi, A. 2001, ApJ, 548, L73
Higdon, S. J. U., Devost, D., Higdon, J. L., et al. 2004, PASP, 116, 975
Hollenbach, D. J, & Tielens, A. G. G. M. 1999, Rev. Mod. Phys., 71, 173
Houck, J. R., Roellig, T. L., van Cleve, J., et al. 2004, ApJS, 154, 18
Houck, J. R., Soifer, B. T., Weedman, D., et al. 2005, ApJ, 622, L105
Houck, J. R., Weedman, D. W., LeFloc'h, E., & Hao, L. 2007, ApJ, 671, 323
Imanishi, M., Dudley, C. C., Maiolino, R., et al. 2007, ApJ, 171, 72
Ivison, R. J., Swinbank, A. M., Swinyard, B., et al. 2010, A&A, 518, L35
Kennicutt, R. C. 1998, ARA&A, 36, 18
Kovacs, A., Omont, A., Beelen, A., et al. 2010, ApJ, 717, 29
Lagache, G., Dole, H., Puget, J.-L., et al. 2004, ApJS, 154, 112
Lebouteiller, V., et al. 2012, A&A, submitted
Lebouteiller, V., Barry, D. J., Bernard-Salas, H., et al. 2011, ApJS, 196, 8
Le Floc'h, E., Papovich, C., Dole, H., et al. 2005, ApJ, 632, 169
Levenson, N. A., Sirocky, M. M., Hao, L., et al. 2007, ApJ, 654, 45
Lonsdale, C. J., Polletta, M. C., Omont, A., et al. 2010, ApJ, 692, 422
Luhman, M. L., Satyapal, S., Fischer, J., et al. 2003, ApJ, 594, 758
Madau, P., Pozzetti, L., & Dickinson, M. 1998, ApJ, 498, 106
Magdis, G. E., Elbaz, D., Hwang, H. S., et al. 2010, MNRAS, 409, 22
Maiolino, R., Cox, P., Caselli, P., et al. 2005, A&A, 440, L51
Malhotra, S., Kaufman, M. J., Hollenbach, D., et al. 2001, ApJ, 561, 766
Meijerink, R., Spaans, M., & Israel, F. P. 2007, A&A, 461, 793
Menendez-Delmestre, K., Blain, A. W., Smail, I., et al. 2009, ApJ, 699, 667
Mookerjea, B., Kramer, C., Buchbender, C., et al. 2011, A&A, 532, 152
Peeters, E., Spoon, H. W. W., & Tielens, A. G. G. M. 2004, ApJ, 613, 986
Pilbratt, G. L., Riedinger, J. R., Passvogel, T., et al. 2010, A&A, 518, L1
Poglitsch, A., Waelkens, C., Geis, N., et al. 2010, A&A, 518, L2
Pope, A., Chary, R.-R., Alexander, D. M., et al. 2008, ApJ, 575, 1171
Reddy, N. A, & Steidel, C. C. 2009, ApJ, 692, 778
Rieke, G. H., Young, E. T., Engelbracht, C. W., et al. 2004, ApJS, 154, 25
Sajina, A., Yan, L., Armus, L., et al. 2007, ApJ, 664, 713
Sanders, D. B., & Mirabel, I. F. 1996, ARA&A, 34, 749
Sargsyan, L. A., Weedman, D. W., & Houck, J. R. 2010, ApJ, 715, 986
Sargsyan, L., Weedman, D., Lebouteiller, V., et al. 2011, ApJ, 730, 19
Smith, J. D. T., Draine, B. T., Dale, D. A., et al. 2007, ApJ, 656, 770
Soifer, B. T., Neugebauer, G., & Houck, J. R. 1987, ARA&A, 25, 187

Spoon, H. W. W., Armus, L., Cami, J., et al. 2004, ApJS, 154, 184
Stacey, G., Geis, N., Genzel, R., et al. 1991, ApJ, 373, 423
Stacey, G., Hailey-Dunsheath, S., Ferkinhoff, C., et al. 2010, ApJ, 724, 957
Tielens, A. G. G. M., & Hollenbach, D. 1985, ApJ, 291, 722
Velusamy, T., Langer, W. D., Pineda, J. L., & Goldsmith, P. F. 2012, A&A, 541, 10
Venemans, B. P., McMahon, R. G., Walter, F., et al. 2011, ApJ, 751, L25
Weedman, D. W, & Houck, J. R. 2008, ApJ, 686, 127
Weedman, D. W, & Houck, J. R. 2009a, ApJ, 693, 370
Weedman, D. W, & Houck, J. R. 2009b, ApJ, 698, 1682
Wright, E. L. 2006, PASP, 118, 1711
Wu, Y., Charmandaris, V., Huang, J., Spinoglio, L., & Tommasin, S. 2009, ApJ, 701, 658
Yan, L., Sajina, A., Fadda, D., et al. 2007, ApJ, 658, 778